Journal of
Marine Science and Engineering

MDPI

Article

Characterizing Gas Hydrate-Bearing Marine Sediments Using Elastic Properties—Part 2: Seismic Inversion Based on a Pore-Filling–Solid Matrix Decoupling Scheme

Zhiqi Guo [1,*], Xiaoyu Lv [1], Cai Liu [1], Haifeng Chen [2] and Lulu Mei [2]

[1] College of Geoexploration Science and Technology, Jilin University, Changchun 130021, China
[2] BGP Inc., CNPC, Zhuozhou 072750, China
* Correspondence: guozhiqi@jlu.edu.cn

Abstract: Characterizing gas hydrate-bearing marine sediments using seismic methods is essential for locating potential hydrate resources. However, most existing pre-stack seismic inversion methods estimate the properties of sediments containing gas hydrates without considering specific characteristics associated with gas hydrate occurrences. In the present study, a pore-filling–solid matrix decoupling amplitude variation with offset (AVO) formula is proposed to represent seismic reflectivity in terms of properties associated with gas hydrates. Based on the rock physics relationships of solid substitution, the parameters introduced into the decoupling AVO equation estimate the concentration of gas hydrates with different occurrences, including pore fillings mixed with water and solid components forming part of the dry sediment frame. A theoretical model test indicates that seismic attributes obtained with the decoupling AVO inversion are superior to the conventional wave velocities-related properties in predicting gas hydrate saturations. A realistic model test further validates the applicability of the proposed method in characterizing a gas hydrate system with varying concentrations and layer thickness. By adjusting the tuning parameters, the configurations and concentrations of the gas hydrate system can be identified using the obtained attributes. Therefore, the presented method provides a useful tool for the characterization of gas hydrate-bearing sediments.

Keywords: pore-filling–solid matrix decoupling AVO equation; solid substitution theory; gas hydrate saturation; gas hydrate occurrence; heterogeneous gas hydrate model

check for updates

Citation: Guo, Z.; Lv, X.; Liu, C.; Chen, H.; Mei, L. Characterizing Gas Hydrate-Bearing Marine Sediments Using Elastic Properties—Part 2: Seismic Inversion Based on a Pore-Filling–Solid Matrix Decoupling Scheme. *J. Mar. Sci. Eng.* **2022**, *10*, 1497. https://doi.org/10.3390/jmse10101497

Academic Editor: Timothy S. Collett

Received: 28 August 2022
Accepted: 13 October 2022
Published: 14 October 2022

1. Introduction

In the accompanying paper (Part 1) [1], we have addressed the rock physics model that quantifies the relationships between gas hydrate occurrence and concentration and the elastic properties of gas hydrate-bearing marine sediments. Using log data, we utilized the proposed model to predict wave velocities and quantitatively estimate the amount of gas hydrate in marine sediments. The model-based method yields results that fit core measurement data well. Nevertheless, identifying gas hydrate deposits with an adequate concentration using seismic methods is essential for locating potential gas hydrate resources over a large area.

Bottom-simulating reflectors (BSRs) represent seismic events generated at the bottom of a gas hydrate formation overlying a partially saturated gas zone [2]. The BSR identified on post-stack seismic profiles is usually used to discriminate the presence of the gas hydrate stability zones [3]. Carcione and Tinivella [4] investigated the amplitude variation with offset (AVO) effects of the BSR by incorporating rock physics modeling for gas hydrate formation. The reflection coefficients of the BSR versus offset were computed and analyzed for varied gas hydrate concentrations. Ecker et al. [5] estimated porosity and hydrate saturation from seismic velocities. Based on stratigraphic interpretation and rock physics modeling, seismic AVO attributes and pre-stack elastic inversion methods have been widely used for the characterization of hydrate formations [6–12]. Meanwhile, the spectral decomposition method was incorporated to improve the identification of the gas hydrate and free gas formations [13]. Seismic attenuation of BSR associated with free gas saturated in the underlying layer has also been used to characterize gas hydrate deposits [14,15]. In addition, Ehsan et al. [16] found that gas hydrate-bearing sediments can simultaneously exhibit high P-wave velocity and anomalously low S-wave velocity, suggesting that Poisson's ratio can be used as an indicator for gas hydrate identification.

Despite these successful applications of seismic methods for the characterization of gas hydrate-bearing formations, more sophisticated seismic methods that consider specific occurrences of gas hydrates are required to improve the estimation of hydrate concentration. As suggested in Part 1, occurrence statuses associated with the dynamic process of gas hydrate accumulation account for particular elastic behaviors of the sediments containing hydrates. However, most existing methods are based on the traditional AVO equations that estimate the properties of the entire rock, which may be inadequate for the estimation of the gas hydrate-related properties. Meanwhile, the AVO equations represented by fluid terms may be workable for oil and gas-bearing reservoirs [17–22] but may be inapplicable for gas hydrate systems. It is because gas hydrates cannot be considered pore fluids. The gas hydrates may exist as pore fillings mixed with water at a relatively low concentration while forming part of the solid phase of the dry sediment frame during the accumulation process with an increasing concentration, as discussed in Part 1.

Therefore, in the present study, we propose a new seismic method for the improved estimation of gas hydrate concentrations. Based on the rock physics relationships of the solid substitution, we propose a pore-filling–solid matrix decoupling AVO formula by extending the conventional reflection coefficients expressed in terms of the fluid term. The decoupling AVO equation is used to represent seismic reflectivity associated with the properties of gas hydrates. Then, the responses of the introduced parameters to gas hydrate saturation are analyzed using the rock physics model proposed in Part 1. Next, seismic attributes obtained based on the decoupling equation are tested for improved characterization of gas hydrate sediments. The accuracy of the decoupling AVO equation and the applicability of the proposed seismic attributes for gas hydrate identification are discussed using a theoretical model. Finally, the sensitivity of the obtained attributes for gas hydrate characterization is investigated using a realistic model of the gas hydrate system.

2. Methods

2.1. Pore-Filling–Solid Matrix Decoupling AVO Equation

As discussed in Part 1 [1], during the accumulation process, gas hydrates exist as pore fillings at low concentrations while forming part of the solid phase of marine sediments with increasing concentrations, as illustrated in Figure 1. Meanwhile, the rock physics model presented in Part 1 suggests that the gas hydrate/water mixture filled in pores of marine sediments can exhibit non-zero rigidity. Therefore, the generalized solid substitution theory [23] was used to model the elastic bulk and shear moduli of gas hydrate-bearing sediment (K_{sat} and μ_{sat}) from those of a dry frame (K_{dry} and μ_{dry}) and gas hydrate/water mixture (K_{mix} and μ_{mix}) as follows:

$$K_{sat} = K_{dry} + \frac{K_{mix}(K_{dry} - K_0)^2}{{K_0}^2\varphi - K_{dry}K_{mix} + K_0K_{mix} - K_0K_{mix}\varphi} = K_{dry} + M_k \tag{1}$$

$$\mu_{sat} = \mu_{dry} + \frac{\mu_{mix}(\mu_{dry} - \mu_0)^2}{{\mu_0}^2\varphi - \mu_{dry}\mu_{mix} + \mu_0\mu_{mix} - \mu_0\mu_{mix}\varphi} = \mu_{dry} + M_\mu \tag{2}$$

where K_0 and μ_0 denote the bulk and shear moduli of the solid matrix, respectively. As illustrated in Figure 1, the solid phase composes minerals below critical gas hydrate saturation S_c and consists of minerals and gas hydrates simultaneously beyond S_c. φ represents the pore space occupied by the gas hydrate/water mixture. Russell et al. [19] proposed the use of the fluid term to describe the difference between the bulk moduli of the saturated rock and the dry frame. Accordingly, we introduced two parameters, M_k and M_μ, to quantify the contribution of gas hydrate/water mixture to the bulk and shear moduli of sediment, respectively.

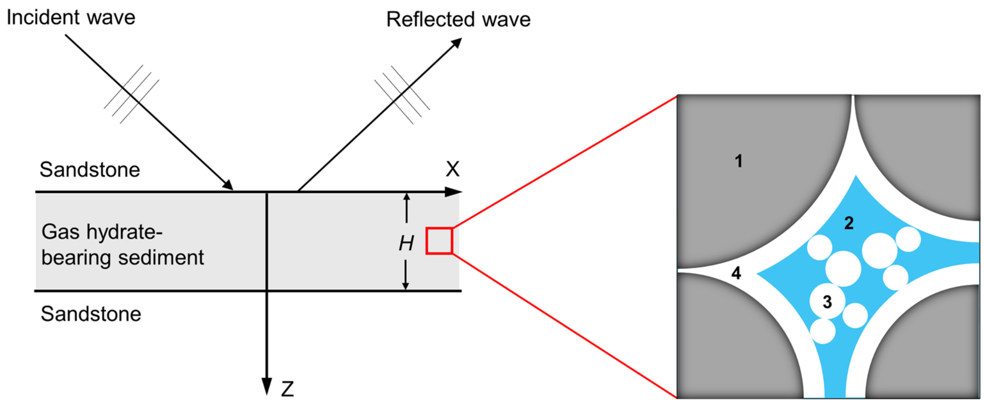

Figure 1. Model for rock physical and seismic modeling where a gas hydrate-bearing sediment is surrounded by sandstones. The rock physics model of the gas hydrate deposit is given in Part 1. 1—Solid frame composed of minerals. 2—Water. 3—Gas hydrates as pore fillings. 4—Gas hydrates as part of the solid frame.

Then, elastic P-wave (V_P) and S-wave (V_S) velocities of the sediment containing gas hydrates can be expressed as follows, referring to Russell et al. [19]:

$$V_P = \sqrt{\left(K_{dry} + \frac{4}{3}\mu_{sat} + M_k\right)/\rho} \tag{3}$$

$$V_S = \sqrt{\left(\mu_{dry} + M_\mu\right)/\rho} \tag{4}$$

where ρ is the bulk density of sediment.

According to Equations (1)–(4), the two parameters for gas hydrate characterization can be represented as follows:

$$M_k = K_{sat} - K_{dry} = \rho V_P^2 - \frac{4}{3}\rho V_S^2 - \left(\gamma_{dry}^2 - \frac{4}{3}\right)\mu_{dry} \tag{5}$$

$$M_\mu = \mu_{sat} - \mu_{dry} = \rho V_S^2 - \mu_{dry} \tag{6}$$

where γ_{dry} represents the P- and S-wave velocity ratio of the dry frame.

Aki and Richards [24] derived the PP-wave reflection coefficient under the assumption of small changes in the elastic properties across an interface between two elastic media:

$$R_{PP}(\theta) = \left(1 + \tan^2\theta\right)\frac{\Delta V_P}{2V_P} + \left(\frac{-8\sin^2\theta}{\gamma_{sat}^2}\right)\frac{\Delta V_S}{2V_S} + \left(1 - \frac{4\sin^2\theta}{\gamma_{sat}^2}\right)\frac{\Delta\rho}{2\rho} \tag{7}$$

where V_P, V_S, and ρ are the averaged velocities and bulk density across the boundary, respectively; ΔV_P, ΔV_S, and $\Delta\rho$ denote the differences in velocities and bulk density across the interface; γ_{sat} represents the P- and S-wave velocity ratio for saturated rock; and θ is the average of the incidence and transmission angles.

Applying the chain rule of the multivariable calculus to Equations (5) and (6) and treating γ_{dry} as a constant can obtain:

$$\Delta M_k = \frac{\partial M_k}{\partial V_P}\Delta V_P + \frac{\partial M_k}{\partial V_S}\Delta V_S + \frac{\partial M_k}{\partial \rho}\Delta\rho + \frac{\partial M_k}{\partial \mu_{dry}}\Delta\mu_{dry} \tag{8}$$

$$\Delta M_\mu = \frac{\partial M_\mu}{\partial V_S}\Delta V_S + \frac{\partial M_\mu}{\partial \rho}\Delta \rho + \frac{\partial M_\mu}{\partial \mu_{dry}}\Delta \mu_{dry} \tag{9}$$

Subsequently, we reparameterized Equation (7) to a new linearized equation using Equations (8) and (9), as follows:

$$\begin{aligned} R_{PP}(\theta) = &\left[\tfrac{1}{4}\left(1-\frac{\gamma_{dry}^2}{\gamma_{sat}^2}\right)\frac{\sec^2\theta}{1+4N/3-\gamma_{dry}^2 N}\right]\frac{\Delta M_k}{M_k} + \left[\left(\frac{N}{3}-\frac{\gamma_{dry}^2 N}{4}\right)\left(1-\frac{\gamma_{dry}^2}{\gamma_{sat}^2}\right)\frac{\sec^2\theta}{1+4N/3-\gamma_{dry}^2 N}\right]\frac{\Delta M_\mu}{M_\mu} \\ &+\left(\frac{\gamma_{dry}^2}{4\gamma_{sat}^2}\sec^2\theta - \frac{2}{\gamma_{sat}^2}\sin^2\theta\right)\frac{\Delta\mu}{\mu} + \left[\tfrac{1}{2}-\tfrac{1}{4}\sec^2\theta\right]\frac{\Delta\rho}{\rho} \end{aligned} \tag{10}$$

where $N = M_\mu/M_k = \left(\mu_{sat}-\mu_{dry}\right)/\left(K_{sat}-K_{dry}\right)$ indicates the contribution ratio of the gas hydrate/water mixture to the shear to bulk modulus of sediment; $\Delta M_k/M_k$ and $\Delta M_\mu/M_\mu$ denote the reflectivity terms associated with the contribution of the gas hydrate/water mixture to the bulk and shear moduli of sediment; $\Delta\mu/\mu$ and $\Delta\rho/\rho$ denote the terms associated with shear modulus and bulk density of sediment, respectively.

Details on the derivations of Equation (10) are illustrated in Appendix A.

2.2. AVO Inversion Based on the Pore-Filling–Solid Matrix Decoupling Scheme

Denoting weighting coefficients in Equation (10) as:

$$\begin{aligned} &A(\theta) = \tfrac{1}{4}\left(1-\frac{\gamma_{dry}^2}{\gamma_{sat}^2}\right)\frac{\sec^2\theta}{1+4N/3-\gamma_{dry}^2 N} \quad B(\theta) = \left(\frac{N}{3}-\frac{\gamma_{dry}^2 N}{4}\right)\left(1-\frac{\gamma_{dry}^2}{\gamma_{sat}^2}\right)\frac{\sec^2\theta}{1+4N/3-\gamma_{dry}^2 N} \\ &C(\theta) = \frac{\gamma_{dry}^2}{4\gamma_{sat}^2}\sec^2\theta - \frac{2}{\gamma_{sat}^2}\sin^2\theta \qquad D(\theta) = \tfrac{1}{2}-\tfrac{1}{4}\sec^2\theta \end{aligned} \tag{11}$$

we simplified Equation (10) as follows:

$$R_{PP}(\theta) = A(\theta)\frac{\Delta M_k}{M_k} + B(\theta)\frac{\Delta M_\mu}{M_\mu} + C(\theta)\frac{\Delta\mu}{\mu} + D(\theta)\frac{\Delta\rho}{\rho} \tag{12}$$

For a pre-stack seismic gather with n incident angles, Equation (12) can be expressed in the matrix as follows:

$$\begin{bmatrix} R_{PP}(\theta_1) \\ R_{PP}(\theta_2) \\ \vdots \\ \vdots \\ R_{PP}(\theta_n) \end{bmatrix} = \begin{bmatrix} A(\theta_1) & B(\theta_1) & C(\theta_1) & D(\theta_1) \\ A(\theta_2) & B(\theta_2) & C(\theta_2) & D(\theta_2) \\ \vdots & \vdots & \vdots & \vdots \\ \vdots & \vdots & \vdots & \vdots \\ A(\theta_n) & B(\theta_n) & C(\theta_n) & D(\theta_n) \end{bmatrix} \begin{bmatrix} \Delta M_k/M_k \\ \Delta M_\mu/M_\mu \\ \Delta\mu/\mu \\ \Delta\rho/\rho \end{bmatrix} \tag{13}$$

Equation (13) can be simplified as:

$$\mathbf{R} = \mathbf{C}\begin{bmatrix} \Delta M_k/M_k \\ \Delta M_\mu/M_\mu \\ \Delta\mu/\mu \\ \Delta\rho/\rho \end{bmatrix} \tag{14}$$

where **R** denotes the reflection coefficient matrix, and **C** is the weighting coefficient matrix in Equation (13).

Finally, the terms in Equation (14) can be estimated using the least-squares method:

$$\begin{bmatrix} \Delta M_k/M_k \\ \Delta M_\mu/M_\mu \\ \Delta\mu/\mu \\ \Delta\rho/\rho \end{bmatrix} = \left(\mathbf{C}^T\mathbf{C} + \varepsilon^2\mathbf{I}\right)^{-1}\mathbf{C}^T R \tag{15}$$

where ε represents the damping factor, and I is the identity matrix.

3. Results

3.1. Elastic Properties and Seismic Responses of Gas Hydrate-Bearing Sediments

Based on the rock physics model in Part 1, we computed the elastic properties of the gas hydrate-bearing layer in Figure 1. Volumetric fractions of minerals were set to 0.60, 0.35, and 0.05 for quartz, clay, and calcite, respectively. Critical gas hydrate saturation S_c was assumed to be 0.1. Other properties used for modeling were the same as those in Part 1.

Figure 2 illustrates the modeled elastic properties of V_P, V_S, and ρ, varying with porosity φ and gas hydrate saturation S_{gh}. As shown in Figure 2a,b, V_P and V_S exhibit subtle variation with S_{gh} for the case of φ lower than ~ 0.2 while rising considerably with S_{gh} for φ higher than ~ 0.2. Since shallow marine sediments are usually unconsolidated and have much higher porosity than 0.2, V_P and V_S are applicable to estimate hydrate concentration. In contrast, ρ of the hydrate deposit is not sensitive to the variation in S_{gh} at all porosity but drops significantly with increasing φ regardless of any S_{gh} (Figure 2c). It implies that density can provide porosity information of gas hydrate deposits, which is significant in estimating hydrate concentration from the saturation value.

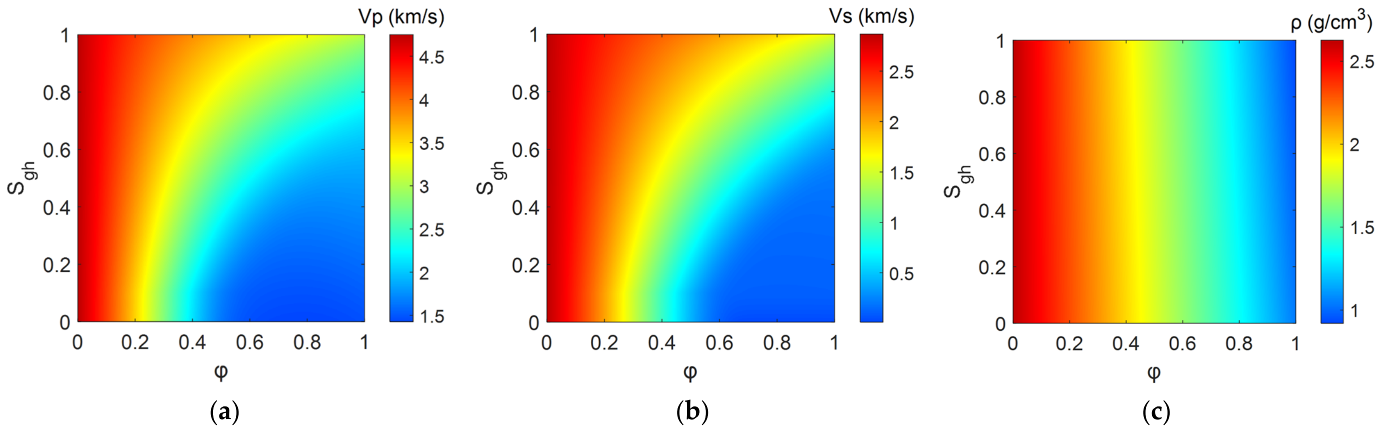

Figure 2. Properties of (**a**) V_p, (**b**) V_s, and (**c**) ρ of marine sediments for varied gas hydrate saturation (S_{gh}) and porosity (φ).

Meanwhile, Figure 3a,b shows the values of M_k and M_μ computed using the relationships presented in Equations (5) and (6). The shear modulus μ of hydrate sediments (Figure 3c) and elastic moduli of the dry frame for computing M_k and M_μ were obtained with the rock physics model presented in Part 1. As illustrated in Figure 3a,b, the variations of M_k and M_μ with S_{gh} and φ are distinct from those of V_P and V_S M_k is sensitive to S_{gh} for φ lower than ~ 0.5, decreasing dramatically with increasing S_{gh} (Figure 3a). At the same time, M_μ increases with S_{gh} at all φ, especially for φ higher than ~ 0.3 (Figure 3b). It implies that M_k and M_μ can provide additional constraints for hydrate characterization besides V_P, V_S, and ρ.

According to the mathematical representations of M_k and M_μ in Equations (5) and (6), the results in Figure 3a,b show that for increasing S_{gh}, pore-filling gas hydrates show less contribution to the bulk modulus of sediments while exhibiting an enhanced influence on shear modulus of sediments. These results deserve further investigation based on petrophysical analyses and laboratory measurements on the accumulation process of gas hydrates formed in ocean bottom sediments. In addition, as can be expected, the shear modulus μ of sediments (Figure 3c) exhibits similar responses to S_{gh} and φ as V_S (Figure 2b).

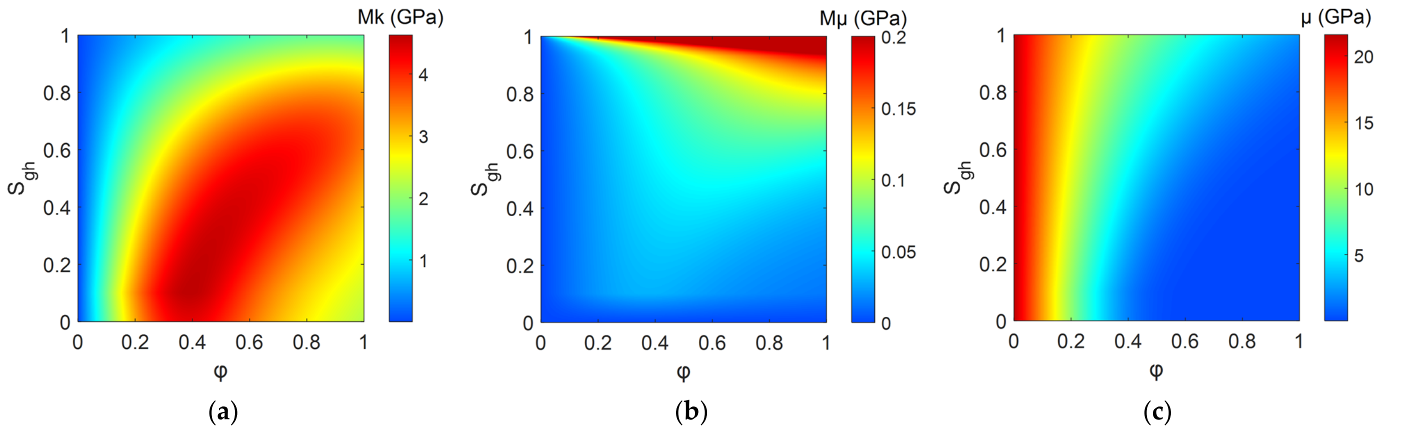

Figure 3. Properties of (**a**) M_k, (**b**) M_μ, and (**c**) μ of marine sediments for varied gas hydrate saturation (S_{gh}) and porosity (φ).

Then, we compute the seismic responses of the model in Figure 1 for the gas hydrate layer with varied S_{gh}. The thickness of the gas hydrate layer was set to 40 m. Porosity is assumed to be 0.4. Other reservoir properties of the gas hydrate sediment are the same as those for rock physics modeling in Figures 2 and 3. Figure 4a illustrates the correlation between V_P and S_{gh} extracted from Figure 2. The surrounding sandstone was assumed to have S_{gh} = 0.1 (equal to the critical hydrate saturation), mimicking the smooth transition of gas hydrate saturation at the boundaries of the gas hydrate layer.

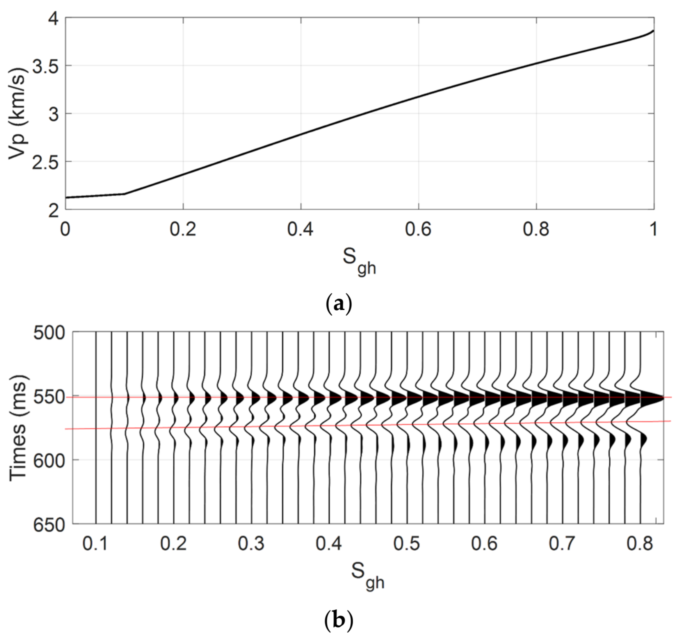

Figure 4. (**a**) V_p for varied S_{gh} in gas hydrate-bearing sediments and (**b**) synthetic seismograms for the model in Figure 1 with S_{gh} varying from 0.1 to 0.8. Two red lines indicate the top and bottom of the gas hydrate layer, respectively.

We used the propagator matrix method (PMM) as a modeling tool to generate synthetic data. The PMM based on Carcione [25] was extended to integrate the rock physics model and compute reflected waveforms, with the details presented by Guo et al. [26,27]. The source Ricker wavelet has a dominant frequency of 40 Hz. The incidence angle ranges from 0° to 30°. The computed AVO gathers were stacked to obtain seismic traces in Figure 4b, showing amplitude variations for S_{gh} varying from 0.1 to 0.8. The computed synthetic seismograms were used to test the proposed pore-filling–solid matrix decoupling AVO inversion method.

3.2. Theoretical Model Test of the Decoupling AVO Inversion

We tested the accuracy of the proposed decoupling AVO equation and its applicability for hydrate characterization using the synthetics of the theoretical model shown in Figure 4. In Equation (10), two parameters, γ_{dry} and N, were introduced into the decoupling AVO formula. Russell et al. [19] treated γ_{dry} as a tuning parameter whose values can best identify gas sands.

Here, to give the initial estimates of γ_{dry} and N in the theoretical model test, the two parameters were simultaneously determined based on the reflection coefficients that were computed by incorporating rock physics modeling. Specifically, we determined the (γ_{dry}, N) values that provide the best accuracy of the decoupling AVO equation for both the top and bottom interfaces of the hydrate layer in Figure 1. The objective function searching for (γ_{dry}, N) is as follows:

$$f_{Top+Bottom}\left(\gamma_{dry}, N\right) = \frac{1}{n}\sum_{i=1}^{n}\left[\begin{array}{l} \left| R_{PP\_Decoupled}\left(\gamma_{dry}, N, \theta_i\right) - R_{PP\_Zoeppritz}\left(\gamma_{dry}, N, \theta_i\right)\right|_{Top} \\ +\left| R_{PP\_Decoupled}\left(\gamma_{dry}, N, \theta_i\right) - R_{PP\_Zoeppritz}\left(\gamma_{dry}, N, \theta_i\right)\right|_{Bottom} \end{array}\right] \tag{16}$$

where the objective function was defined as the absolute differences in the PP-wave reflection coefficients between the proposed decoupling AVO equation and the exact Zoeppritz equation at the top and bottom interfaces simultaneously. The incidence angles range from 0° to 30°.

The straightforward grid-search approach was used to find (γ_{dry}, N) in Equation (16). For the model where S_{gh} of the hydrate layer was set to have a typical value of 0.3 and other properties were given in Section 3.1, we had the estimated (γ_{dry}, N) values of (1.70, 0.02). Corresponding curves for analyzing the accuracy of the decoupling AVO equation is shown in Figure 5. The results indicate the obtained (γ_{dry}, N) values can provide AVO curves with reasonable accuracy for the model.

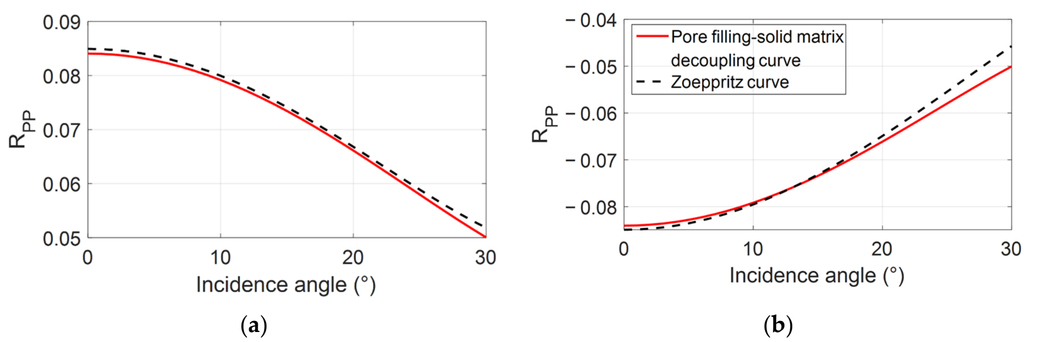

Figure 5. Comparison between the PP-wave reflection coefficients obtained with the Zoeppritz equation (black dashed curves) and the pore-filling–solid matrix decoupling AVO equation (red solid curves) for the (**a**) top and (**b**) bottom interfaces of the gas hydrate layer in Figure 1.

Then, using the synthetic data in Figure 4b and the estimated values of (γ_{dry}, N), we performed AVO inversion and compared the results obtained using the proposed decoupling method with those computed based on the Aki and Richards formula in Equation (7). Figure 6 illustrates $\Delta M_k/M_k$, $\Delta M_\mu/M_\mu$, $\Delta\mu/\mu$, and $\Delta\rho/\rho$ computed using the straightforward AVO inversion based on the decoupling scheme presented in Section 2.2. For comparison, as shown in Figure 7, we displayed $\Delta V_P/V_P$, $\Delta V_S/V_S$, and $\Delta\rho/\rho$ inverted based on Equation (7), following the scheme similar to that in Section 2.2.

=

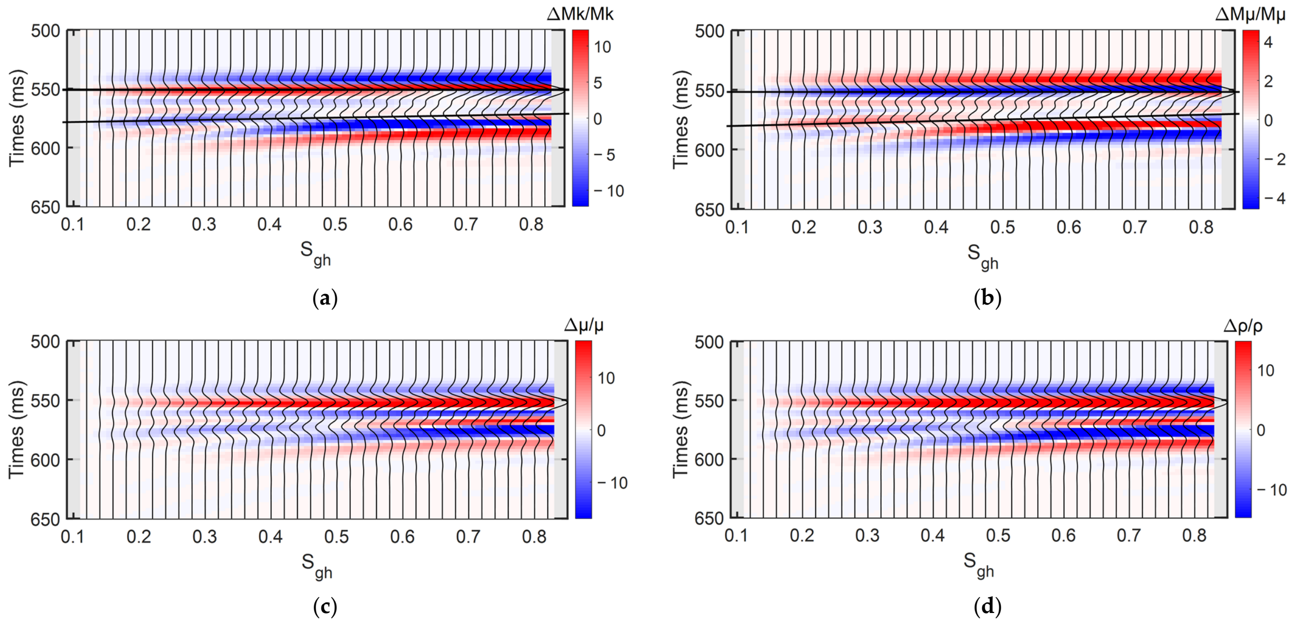

Figure 6. Inverted results of (**a**) $\Delta M_k/M_k$, (**b**) $\Delta M_\mu/M_\mu$, (**c**) $\Delta\mu/\mu$, and (**d**) $\Delta\rho/\rho$ for varied S_{gh} using the pore-filling–solid matrix decoupling method in Equation (10). Two black lines indicate the top and bottom of the gas hydrate layer, respectively.

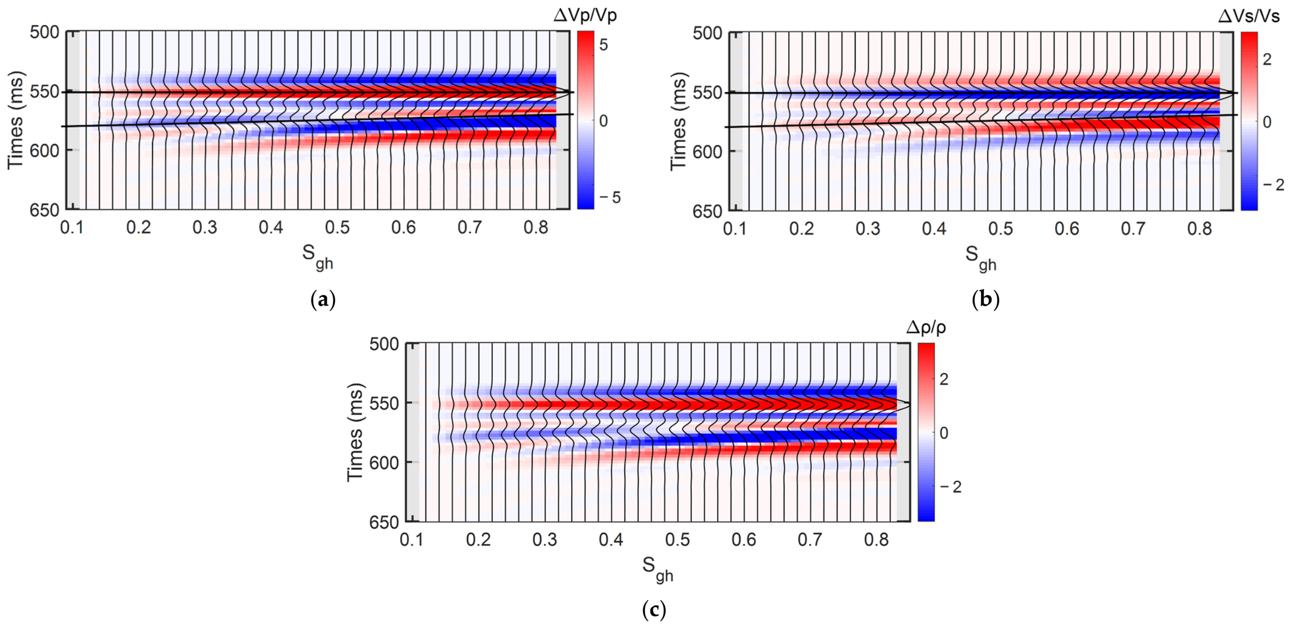

Figure 7. Inverted results of (**a**) $\Delta V_P/V_P$, (**b**) $\Delta V_S/V_S$, and (**c**) $\Delta\rho/\rho$ for varied S_{gh} using Aki and Richards formula in Equation (7). Two black lines indicate the top and bottom of the hydrate layer, respectively.

Compared to $\Delta V_P/V_P$ and $\Delta V_P/V_S$ (Figure 7a,b), $\Delta M_k/M_k$ and $\Delta M_\mu/M_\mu$ (Figure 6a,b) show similar anomaly responses to the increase in S_{gh} at the top and bottom interfaces of the gas hydrate layer. Most importantly, $\Delta M_k/M_k$ and $\Delta M_\mu/M_\mu$ exhibit fewer ambiguities irrelevant to S_{gh} variations within the gas hydrate layer. The results suggest that the hydrate-related attributes ($\Delta M_k/M_k$ and $\Delta M_\mu/M_\mu$) exhibit the potential to provide more reliable estimates of gas hydrate saturation than the traditional wave velocities-related properties ($\Delta V_P/V_P$ and $\Delta V_S/V_S$).

Meanwhile, $\Delta\mu/\mu$ (Figure 6c) shows the anomalies comparable to those provided by $\Delta V_S/V_S$ (Figure 7b) for increasing S_{gh}, revealing gas hydrates existing as part of the solid component can enhance the rigidity of sediments. In addition, $\Delta\rho/\rho$ obtained with the two methods (Figures 6d and 7c) show consistent responses, suggesting the robustness of the inversion based on the decoupling AVO equation.

3.3. Realistic Model Test of the Decoupling AVO Inversion

As illustrated by the V_P profile in Figure 8a, a realistic model of the gas hydrate system was designed referring to the seismic interpretation in Yang et al. [28], where a gas hydrate deposit with higher wave velocities is formed in shallow ocean-bottom sediments. In the model, the gas hydrate-bearing sediment has a relatively larger thickness centered at trace number 40 and pinching towards two sides. Meanwhile, S_{gh} of gas hydrate sediment is set to 0.6 in the center and linearly drops to 0.2 at the two edges laterally. Thus, the model delineates the gas hydrate formation with varied thicknesses and gas hydrate concentrations. φ and S_c of the gas hydrate deposit were set to 0.5 and 0.1, respectively. Based on the properties used in Section 3.1, elastic properties of the gas hydrate sediment for varied S_{gh} values were computed based on the rock physics model proposed in Part 1.

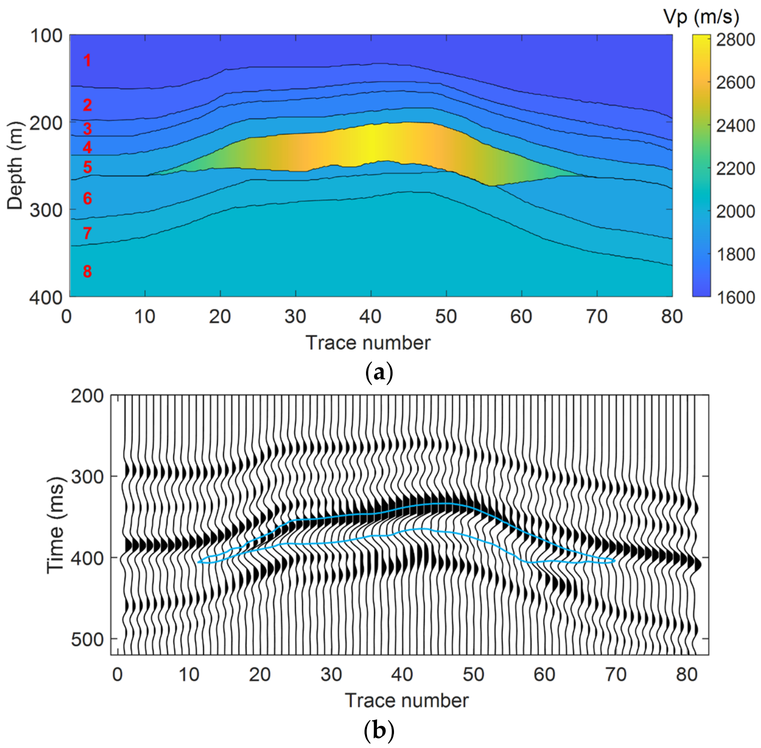

Figure 8. (**a**) V_P profile showing a geological model of gas hydrate system formed in the layered marine sediments, where S_{gh} decreases from the center to edges on both sides in the gas hydrate layer and (**b**) corresponding post-stack seismic section computed with the propagator matrix method, with the interpreted outline of the gas hydrate formation indicated in blue.

The elastic properties of the shallow marine formations are given in Table 1, according to Yang et al. [28]. Meanwhile, shear wave velocities of the marine sediments were estimated using a constant V_P/V_S ratio of 3. The source Ricker wavelet has a dominant frequency of 20 Hz. The incidence angle ranges from 0° to 30°. Using the PMM as a modeling tool, we computed the synthetic AVO data for the model in Figure 8a, with the corresponding post-stack seismic section illustrated in Figure 8b. The boundary of the gas hydrate formation was outlined, characterized by the positive and negative reflections at the top and bottom interfaces, respectively. The reflection amplitude strength fades from the center towards the two ends of the gas hydrate layer, interpreted by the decrease in wave velocities of the gas hydrate formation owing to the decrease in S_{gh}. Limitations of seismic resolution and interferences associated with the layered sediments may increase uncertainty in structural interpretation and S_{gh} estimations for the gas hydrate deposits.

Table 1. Elastic properties of the ocean-bottom formations in the realistic model in Figure 8a.

VP **(m/s)**	ρ **(kg/m^3)**
1600	1740
1680	1760
1740	1770
1790	1790
1935	1870
1940	1880
2000	1920
2040	1940

Figure 9 demonstrates three pre-stack AVO gathers for the models at different trace numbers in Figure 8. The red lines denote the top and bottom of the gas hydrate formation. It is evident that AVO signatures vary considerably with S_{gh} and layer thickness. Phase reversal is observed for the bottom reflection of the gas hydrate formation at trace numbers 40 and 50, which may explain the relatively weak seismic responses at these locations on the post-stack profile (Figure 8b). Most importantly, it implies that we may expect additional information not revealed in the post-stack section but can be obtained with pre-stack inversion. Next, the synthetics are used to test the decoupling AVO inversion.

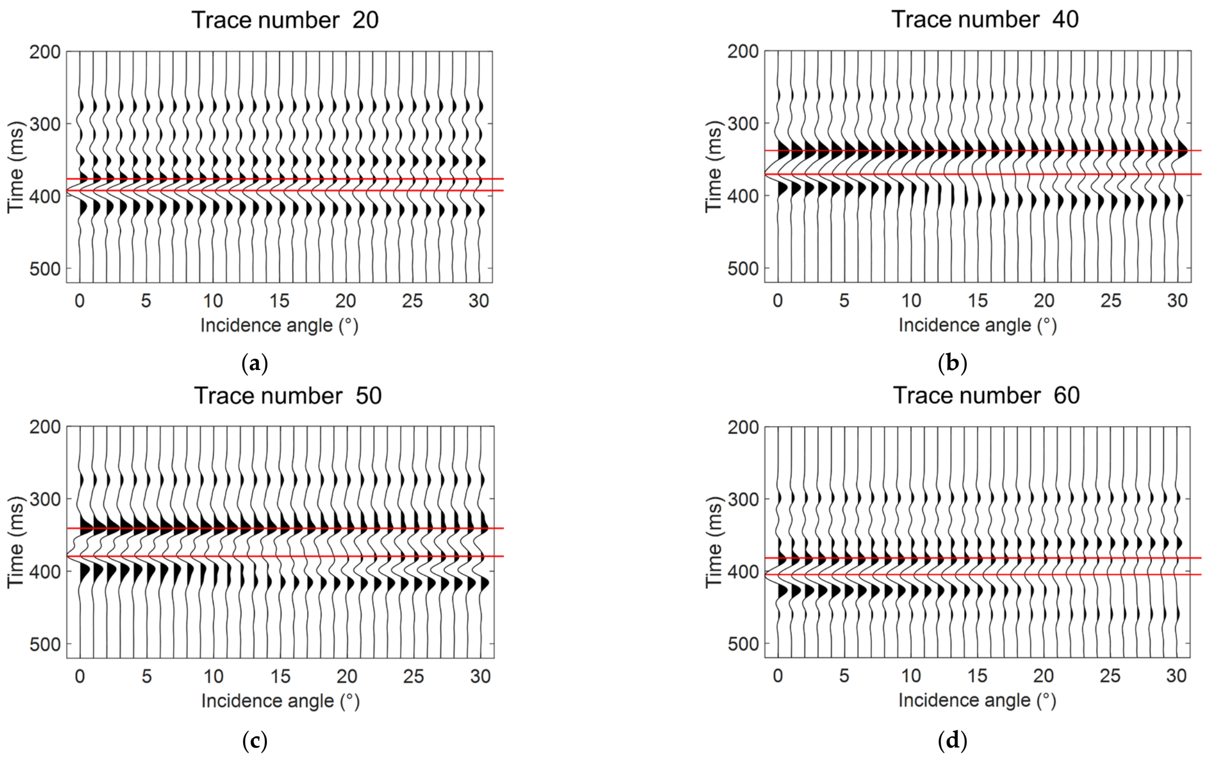

Figure 9. Pre-stack AVO synthetics from the models in Figure 8 at traces with the numbers (**a**) 20, (**b**) 40, (**c**) 50, and (**d**) 60, respectively. The red lines indicate the top and bottom of the gas hydrate-bearing formation.

We then applied the proposed decoupling AVO inversion method to the synthetic AVO data of the gas hydrate model in Figure 8. Based on the procedure presented in Section 3.2 and using the gas hydrate layer with S_{gh} = 0.3 as the reference model, we obtained the (γ_{dry}, N) values of (1.90, 0.06) as initial estimates of the adjusting parameters, which were used in the decoupling AVO inversion.

Figure 10a,b illustrate the sections of $\Delta V_P/V_P$ and $\Delta V_S/V_S$ that were computed based on Equation (7), respectively. The values of $\Delta V_P/V_P$ were normalized to the range between -1 and 1. In Figure 10b, $\Delta V_S/V_S$ shows a relatively higher magnitude than $\Delta V_P/V_P$ while retaining the relative difference between them, which is consistent with the analysis of the reflectivity across interfaces of the model. Meanwhile, the responses of $\Delta V_P/V_P$ and $\Delta V_S/V_S$ to the hydrate system are similar.

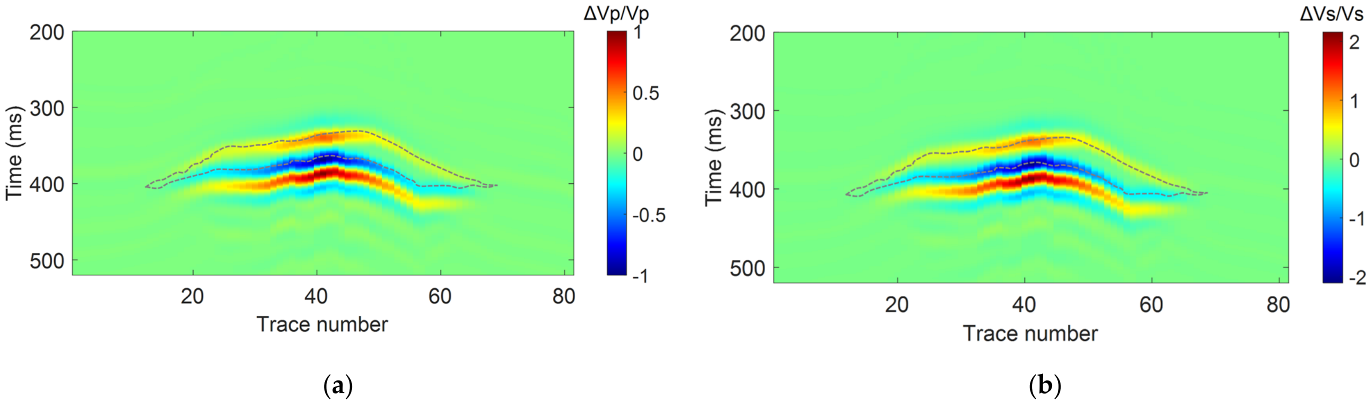

Figure 10. Results of (**a**) $\Delta V_P/V_P$ and (**b**) $\Delta V_S/V_S$ inverted based on the conventional AVO formula in Equation (7) for the model of the gas hydrate system in Figure 8.

Results indicate that the boundary of the gas hydrate layer can be approximately discriminated on the $\Delta V_P/V_P$ section (Figure 10a). Compared with the post-stack section (Figure 8b), the bottom of the hydrate layer exhibits more visibility in the $\Delta V_P/V_P$ section, indicating the seismic attributes obtained from AVO effects can improve the characterization of the hydrate system. Meanwhile, the decrease in S_{gh} from the center to the two sides can be identified by the decrease in $\Delta V_P/V_P$ for both the top and bottom interfaces. However, the $\Delta V_P/V_P$ anomalies tend to weaken dramatically to the two edges of the gas hydrate layer with a smaller thickness and lower S_{gh}, which may account for the uncertainty in the gas hydrate interpretation.

In comparison, Figure 11 shows the sections of $\Delta M_k/M_k$ obtained with the decoupling AVO scheme. We focused on analyzing $\Delta M_k/M_k$ while not displaying the sections of $\Delta M_\mu/M_\mu$ for simplicity since they show similar distributions for the gas hydrate system. In practice, we found that for similar values of N within the magnitude of the value estimated above, the influence of the parameter N is not significant, primarily influencing the magnitude of the obtained results. Therefore, we kept N at the value of 0.06, as estimated for the reference model. Subsequently, we regarded γ_{dry} as a tuning parameter and tested its impact on the obtained results. As shown in Figure 11, for γ_{dry} increasing from 1.80, 1.90, 2.10, to 2.20, the visibility of the top interface on the $\Delta M_k/M_k$ section was enhanced. For γ_{dry} at 2.20 (Figure 11d), it achieves a result comparable to that given by $\Delta V_P/V_P$.

Comparing Figures 10 and 11, $\Delta M_k/M_k$ can delineate the bottom of the hydrate layer more clearly than $\Delta V_P/V_P$, especially at the lower γ_{dry} values. In contrast, $\Delta V_P/V_P$ cannot reveal the base of the gas hydrate layer at the two edges with a smaller thickness and lower concentration. Meanwhile, lateral variation of the $\Delta M_k/M_k$ value positively correlates with S_{gh}. Therefore, by adjusting the tuning parameter γ_{dry}, $\Delta M_k/M_k$ acts as a superior indicator for identifying the configurations and concentrations of the gas hydrate system. However, the implications of the tradeoff between the performance of $\Delta M_k/M_k$ for characterizing the top and bottom boundaries of the gas hydrate layer have not been fully understood.

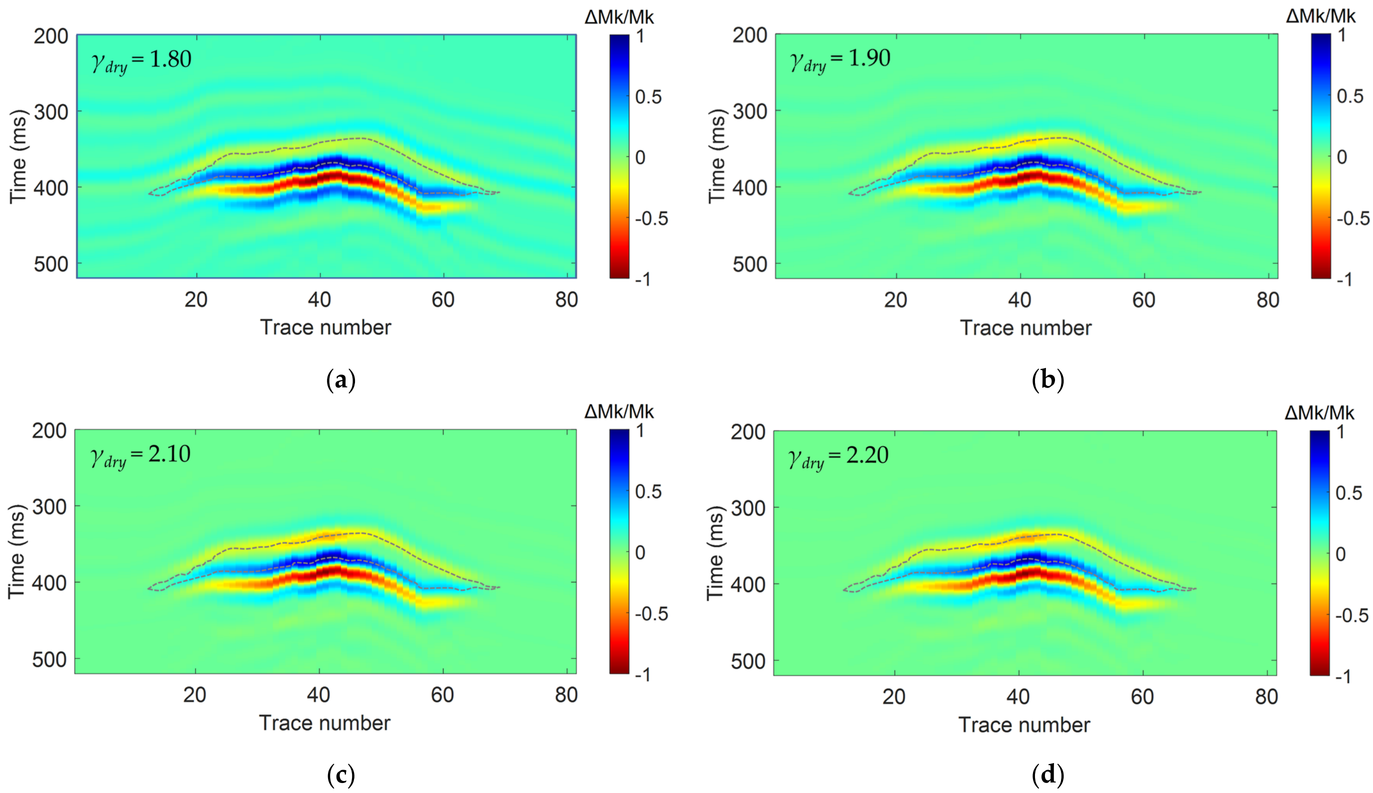

Figure 11. Results of $\Delta M_k/M_k$ inverted based on the pore-filling–solid matrix decoupling AVO formula in Equation (10) for the model of the gas hydrate system in Figure 8. The tuning parameter γ_{dry} is tested using the values of (**a**) 1.80, (**b**) 1.90, (**c**) 2.10, and (**d**) 2.20, respectively.

4. Discussion

We have proposed a pore-filling–solid matrix decoupling AVO formula to represent seismic reflectivity in terms of properties associated with gas hydrates. The proposed equation can be regarded as the generalization of the popular AVO expressions in terms of fluid factors [19–22]. One of the advantages of the proposed decoupling formula in the present study is to model seismic signatures associated with the pore-filled mixture of gas hydrate and water that exhibit non-zero rigidity, which is not considered by most existing methods. Moreover, inversion of the introduced parameters with the decoupling AVO equation enables direct estimations of gas hydrate concentrations with different occurrences, including pore fillings and solid components of the sediment frame.

The results of a theoretical model test suggest that the gas hydrate-related attributes ($\Delta M_k/M_k$ and $\Delta M_\mu/M_\mu$) exhibit more evident anomalies to the variation in S_{gh} for a gas hydrate model than the traditional wave velocities-related properties ($\Delta V_P/V_P$ and $\Delta V_S/V_S$), therefore improving the characterization of gas hydrate-bearing sediments (Figures 6 and 7). The test using a realistic model further confirms the superiority of the decoupling AVO inversion in the characterization of a gas hydrate system with heterogeneous concentrations and varied layer thickness (Figures 10 and 11).

The modeling results of synthetic data (Figures 8b and 9) indicate that the gas hydrate system exhibits particular AVO effects. Phase reversal can be observed in the events of bottom reflections in the computed pre-stack angle gathers, especially for the gas hydrate layer with a larger thickness and higher concentrations (Figure 9b,c). Such phase reversal accounts for the weak seismic responses at corresponding locations on the post-stack profile (Figure 8b), challenging the accurate identification of the gas hydrate system. However, the proposed decoupling inversion can capture properties of the gas hydrate system revealed by such AVO effects, with the gas hydrate distribution identified in the $\Delta M_k/M_k$ section (Figure 11).

Nevertheless, the successful identification of gas hydrate depends on appropriate tuning parameter values. We used the approach demonstrated in Section 3.2 to obtain the initial estimates of the tuning parameters (γ_{dry}, N). Test results indicate that γ_{dry} is a critical tuning parameter that determines the performance of the gas hydrate-related attributes. By adjusting the tuning parameters, the proposed attributes can delineate the configurations and concentrations of the hydrate system. However, the tradeoff features of the proposed attributes in characterizing the top and bottom boundaries of the hydrate layer (Figure 11) have not been thoroughly understood. It deserves further investigation based on laboratory measurement and rock physics modeling. Meanwhile, owing to the particular characteristics of the gas hydrate-bearing marine sediments, the range of the γ_{dry} value should be determined based on future rock physics studies.

As illustrated in Section 2.2, we have performed straightforward inversion using the least-squares method using the decoupling AVO equation without the constraints from log data. It can mimic the marine seismic survey at the predrilling exploration stage with no boreholes drilled. Meanwhile, accurate estimations of gas hydrate-related properties remain challenging even in the presence of adequate log data, owing to the insufficient understanding of the rock properties of hydrate sediments.

The merit of the present study is proposing a pore-filling–solid matrix decoupling AVO equation, which is applicable for hydrocarbon reservoirs where pore fillings should be regarded as solid components. The decoupling method can be further extended based on the elastic impedance inversion scheme while using log data as constraints. At the same time, based on a better understanding of the seismic attenuation of BSR [14,15] and poroelastic behaviors of the gas hydrate layer [29–33], the decoupling AVO equation can be transformed into the frequency domain to estimate dispersion attributes for improved gas hydrate characterization. Meanwhile, based on appropriate rock physics modeling methods, the influence of free gas should be considered for better descriptions of the poroelastic behaviors of the gas hydrate-bearing sediments and corresponding seismic signatures. In addition, the decoupling equation and its potential extensions can be further applied when real seismic data are available.

5. Conclusions

A pore-filling–solid matrix decoupling AVO method was proposed to represent seismic reflectivity in terms of properties associated with gas hydrates. Based on the rock physics relationships of solid substitution, the decoupling AVO equation was established by extending the popular reflection coefficients represented by fluid terms. The decoupling AVO method estimates gas hydrate concentrations with various occurrences through the introduced parameters that evaluate the effect of pore-filled gas hydrates and the gas hydrates as part of the dry frame on elastic moduli of marine sediments. Therefore, the presented method provides a way to estimate the gas hydrate concentration directly while considering the occurrences. A theoretical model test indicates that seismic attributes obtained with the decoupling AVO inversion exhibit superiority in estimating gas hydrate saturations compared to the conventional seismic properties associated with wave velocities. Furthermore, a realistic model test validates the applicability of the decoupling method for the characterization of a gas hydrate system with heterogeneous concentrations and varied layer thickness. The proposed attributes can delineate the configurations and concentration variations of the gas hydrate system by adjusting the tuning parameters. Therefore, the presented method provides a useful seismic method for improved characterization of gas hydrate-bearing marine sediments using elastic properties.

Future studies may include extending the decoupling AVO formula based on the elastic impedance inversion scheme and using rock physics modeling results from log data as constraints in the inversion. Meanwhile, the decoupling AVO equation can be transformed into the frequency-dependent formula to estimate associated dispersion attributes. Finally, the decoupling AVO method and its potential extensions can be generalized for the characterization of other hydrocarbon resources when pore fillings in reservoirs should be treated as solid components and described using the solid substitution model accordingly.

Author Contributions: Conceptualization, Z.G.; methodology, Z.G. and X.L.; software, X.L.; validation, Z.G. and X.L.; formal analysis, Z.G. and X.L.; investigation, Z.G. and H.C.; resources, C.L.; data curation, H.C. and L.M.; writing—original draft preparation, Z.G.; writing—review and editing, Z.G.; visualization, X.L.; project administration, Z.G.; funding acquisition, Z.G. All authors have read and agreed to the published version of the manuscript.

Funding: This research was funded by the National Natural Science Foundation of China (grant numbers 42074153 and 42274160) and the CNPC Science Research and Technology Development Project (grant number 2021DJ3503).

Institutional Review Board Statement: Not applicable.

Informed Consent Statement: Not applicable.

Data Availability Statement: All data have been provided in the paper.

Conflicts of Interest: The authors declare no conflict of interest.

Appendix A

We presented the derivation of the pore-filling–solid matrix decoupling AVO equation in detail. First, we rewrite the Aki–Richards equation, Equation (7), with a common denominator of $\rho {V_P}^2$:

$$R_{PP}(\theta) = \left[\frac{1}{2}\Delta\rho V_P^2 + \frac{1}{2}\rho V_P \Delta V_P \sec^2\theta - 2\left(\Delta\rho V_S^2 + 2\rho V_S \Delta V_S\right)\sin^2\theta\right] / \rho V_P^2 \tag{A1}$$

here, we rewrote the two proposed parameters M_k and M_μ in Equations (5) and (6):

$$M_k = K_{sat} - K_{dry} = \rho V_P^2 - \frac{4}{3}\rho V_S^2 - \left(\gamma_{dry}^2 - \frac{4}{3}\right)\mu_{dry} \tag{A2}$$

$$M_\mu = \mu_{sat} - \mu_{dry} = \rho V_S^2 - \mu_{dry} \tag{A3}$$

and corresponding chain rules in Equations (8) and (9) as follows:

$$\Delta M_k = \frac{\partial M_k}{\partial V_P}\Delta V_P + \frac{\partial M_k}{\partial V_S}\Delta V_S + \frac{\partial M_k}{\partial \rho}\Delta\rho + \frac{\partial M_k}{\partial \mu_{dry}}\Delta\mu_{dry} \tag{A4}$$

$$\Delta M_\mu = \frac{\partial M_\mu}{\partial V_S}\Delta V_S + \frac{\partial M_\mu}{\partial \rho}\Delta\rho + \frac{\partial M_\mu}{\partial \mu_{dry}}\Delta\mu_{dry} \tag{A5}$$

Applying Equations (A4) and (A5) in Equations (A2) and (A3) generates:

$$\Delta M_k = 2\rho V_P \Delta V_P + V_P^2\Delta\rho - \frac{4}{3}\left(\Delta\rho V_S^2 + 2\rho V_S \Delta V_S\right) - \left(\gamma_{dry}^2 - \frac{4}{3}\right)\Delta\mu_{dry} \tag{A6}$$

$$\Delta M_\mu = \Delta\rho V_S^2 + 2\rho V_S \Delta V_S - \Delta\mu_{dry} \tag{A7}$$

We rearranged Equations (A6) and (A7) as:

$$\Delta\rho V_S^2 + 2\rho V_S \Delta V_S = \Delta M_\mu + \Delta\mu_{dry} \tag{A8}$$

$$\rho V_p \Delta V_P = \frac{1}{2}\left(\Delta M_k - V_P^2\Delta\rho + \frac{4}{3}\Delta M_\mu + \gamma_{dry}^2\Delta\mu_{dry}\right) \tag{A9}$$

and substituted Equations (A8) and (A9) into Equation (A1) to obtain:

$$\begin{aligned} R_{PP}(\theta) = &\left(\tfrac{1}{4}\sec^2\theta\right)\tfrac{\Delta M_k}{\rho V_P^2} + \left(\tfrac{1}{3}\sec^2\theta - 2\sin^2\theta\right)\tfrac{\Delta M_\mu}{\rho V_P^2} \\ &+ \left(\tfrac{1}{4}\gamma_{dry}^2\sec^2\theta - 2\sin^2\theta\right)\tfrac{\Delta\mu_{dry}}{\rho V_P^2} + \left(\tfrac{1}{2} - \tfrac{1}{4}\sec^2\theta\right)\tfrac{\Delta\rho}{\rho} \end{aligned} \tag{A10}$$

We have μ_{dry} = $\mu_{sat} - M_\mu$ according to Equation (A3) and then rearranged Equation (A10) by setting μ = μ_{sat} (neglecting the subscript "*sat*" for simplicity) as follows:

$$\begin{aligned} R_{PP}(\theta) = &\left(\tfrac{1}{4}\sec^2\theta\right)\tfrac{\Delta M_k}{\rho V_P^2} + \left[\left(\tfrac{1}{3} - \tfrac{\gamma_{dry}^2}{4}\right)\sec^2\theta\right]\tfrac{\Delta M_\mu}{\rho V_P^2} \\ &+ \left(\tfrac{\gamma_{dry}^2}{4}\sec^2\theta - 2\sin^2\theta\right)\tfrac{\Delta\mu}{\rho V_P^2} + \left(\tfrac{1}{2} - \tfrac{1}{4}\sec^2\theta\right)\tfrac{\Delta\rho}{\rho} \end{aligned} \tag{A11}$$

Dividing both sides of Equations (A2) and (A3) by $\rho V_P{}^2$ produces:

$$\frac{M_k}{\rho V_P^2} = 1 - \frac{4V_S^2}{3V_P^2} - \left(\gamma_{dry}^2 - \frac{4}{3}\right)\frac{\mu_{dry}}{\rho V_P^2} = 1 - \frac{4}{3\gamma_{sat}^2} - \left(\gamma_{dry}^2 - \frac{4}{3}\right)\frac{\mu_{dry}}{\rho V_P^2} \tag{A12}$$

$$\frac{M_\mu}{\rho V_P^2} = \frac{V_S^2}{V_P^2} - \frac{\mu_{dry}}{\rho V_P^2} = \frac{1}{\gamma_{sat}^2} - \frac{\mu_{dry}}{\rho V_P^2} \tag{A13}$$

Substituting Equation (A13) into Equation (A12) gives

$$\frac{M_k}{\rho V_P^2} = 1 - \frac{4M_\mu}{3\rho V_P^2} - \gamma_{dry}^2\frac{\mu_{dry}}{\rho V_P^2} \tag{A14}$$

Using μ_{dry} = $\mu_{sat} - M_\mu$ = $\rho V_S{}^2 - M_\mu$, we rearranged Equation (A14) as:

$$\frac{M_k}{\rho V_P^2} = 1 - \frac{4M_\mu}{3\rho V_P^2} - \gamma_{dry}^2\frac{\rho V_S^2}{\rho V_P^2} + \gamma_{dry}^2\frac{M_\mu}{\rho V_P^2} = 1 - \frac{\gamma_{dry}^2}{\gamma_{sat}^2} + \left(\gamma_{dry}^2 - \frac{4}{3}\right)\frac{M_\mu}{\rho V_P^2} \tag{A15}$$

and further rearranged Equation (A15) as:

$$\frac{1}{\rho V_P^2} = \left[1 - \frac{\gamma_{dry}^2}{\gamma_{sat}^2}\right] / \left[M_k + \frac{4}{3}M_\mu - \gamma_{dry}^2 M_\mu\right] \tag{A16}$$

Substituting Equation (A16) into the M_k and M_μ terms in Equation (A11) gives

$$\begin{aligned} R_{PP}(\theta) = &\left[\left(1 - \tfrac{\gamma_{dry}^2}{\gamma_{sat}^2}\right)\tfrac{1}{4}\sec^2\theta\right]\tfrac{\Delta M_k}{M_k + \frac{4}{3}M_\mu - \gamma_{dry}^2 M_\mu} + \left[\left(\tfrac{1}{3} - \tfrac{\gamma_{dry}^2}{4}\right)\left(1 - \tfrac{\gamma_{dry}^2}{\gamma_{sat}^2}\right)\sec^2\theta\right]\tfrac{\Delta M_\mu}{M_k + \frac{4}{3}M_\mu - \gamma_{dry}^2 M_\mu} \\ &+ \left(\tfrac{\gamma_{dry}^2}{4}\sec^2\theta - 2\sin^2\theta\right)\tfrac{\Delta\mu}{\rho V_P^2} + \left[\tfrac{1}{2} - \tfrac{1}{4}\sec^2\theta\right]\tfrac{\Delta\rho}{\rho} \end{aligned} \tag{A17}$$

Equation (A17) can be further rearranged using $\rho V_P{}^2$ = $\gamma_{sat}{}^2\rho V_S{}^2$ = $\gamma_{sat}{}^2\mu$ as follows:

$$\begin{aligned} R_{PP}(\theta) = &\left[\left(1 - \tfrac{\gamma_{dry}^2}{\gamma_{sat}^2}\right)\tfrac{1}{4}\sec^2\theta\right]\tfrac{\Delta M_k}{M_k + \frac{4}{3}M_\mu - \gamma_{dry}^2 M_\mu} + \left[\left(\tfrac{1}{3} - \tfrac{\gamma_{dry}^2}{4}\right)\left(1 - \tfrac{\gamma_{dry}^2}{\gamma_{sat}^2}\right)\sec^2\theta\right]\tfrac{\Delta M_\mu}{M_k + \frac{4}{3}M_\mu - \gamma_{dry}^2 M_\mu} \\ &+ \left(\tfrac{\gamma_{dry}^2}{4\gamma_{sat}^2}\sec^2\theta - \tfrac{2}{\gamma_{sat}^2}\sin^2\theta\right)\tfrac{\Delta\mu}{\mu} + \left[\tfrac{1}{2} - \tfrac{1}{4}\sec^2\theta\right]\tfrac{\Delta\rho}{\rho} \end{aligned} \tag{A18}$$

By introducing a factor N = M_μ/M_k to rearrange Equation (A18), we obtained the final form of the proposed pore-filling–solid matrix decoupling AVO equation:

$$\begin{aligned} R_{PP}(\theta) = &\left[\tfrac{1}{4}\left(1 - \tfrac{\gamma_{dry}^2}{\gamma_{sat}^2}\right)\tfrac{\sec^2\theta}{1+4N/3-\gamma_{dry}^2 N}\right]\tfrac{\Delta M_k}{M_k} + \left[\left(\tfrac{N}{3} - \tfrac{\gamma_{dry}^2 N}{4}\right)\left(1 - \tfrac{\gamma_{dry}^2}{\gamma_{sat}^2}\right)\tfrac{\sec^2\theta}{1+4N/3-\gamma_{dry}^2 N}\right]\tfrac{\Delta M_\mu}{M_\mu} \\ &+ \left(\tfrac{\gamma_{dry}^2}{4\gamma_{sat}^2}\sec^2\theta - \tfrac{2}{\gamma_{sat}^2}\sin^2\theta\right)\tfrac{\Delta\mu}{\mu} + \left[\tfrac{1}{2} - \tfrac{1}{4}\sec^2\theta\right]\tfrac{\Delta\rho}{\rho} \end{aligned} \tag{A19}$$

We have $M_\mu = 0$ for the case of fluid saturation ($\mu_{dry} = \mu_{sat}$) according to Equation (A3). In this case, the factor $N = M_\mu/M_k$ becomes zero, making Equation (A19) rigorously limited to the form given by Russell et al. [19]:

$$R_{PP}(\theta) = \left[\frac{1}{4}\left(1 - \frac{\gamma_{dry}^2}{\gamma_{sat}^2}\right)\sec^2\theta\right]\frac{\Delta M_k}{M_k} + \left(\frac{\gamma_{dry}^2}{4\gamma_{sat}^2}\sec^2\theta - \frac{2}{\gamma_{sat}^2}\sin^2\theta\right)\frac{\Delta\mu}{\mu} + \left[\frac{1}{2} - \frac{1}{4}\sec^2\theta\right]\frac{\Delta\rho}{\rho} \tag{A20}$$

where the term $\Delta M_k/M_k$ is the same as the fluid term $\Delta f/f$ in Russell et al. [19].

References

1. Guo, Z.Q.; Lv, X.Y.; Liu, C.; Chen, H.F.; Cai, Z.G. Characterizing gas hydrate–bearing marine sediments using elastic properties—Part 1: Rock physical modeling and inversion from well logs. *J. Mar. Sci. Eng.* **2022**, *10*, 1379. [CrossRef]
2. Andreassen, K.; Hogstad, K.; Berteussen, K.A. Gas hydrate in the southern Barents Sea indicated by a shallow seismic anomaly. *First Break* **1990**, *8*, 235–245. [CrossRef]
3. Andreassen, K.; Hartb, P.E.; MacKayc, M. Amplitude versus offset modeling of the bottom simulating reflection associated with submarine gas hydrates. *Mar. Geol.* **1997**, *137*, 25–40. [CrossRef]
4. Carcione, J.M.; Tinivella, U. Bottom simulating reflectors: Seismic velocities and AVO effects. *Geophysics* **2000**, *65*, 54–67. [CrossRef]
5. Ecker, C.; Dvorkin, J.; Nur, A.M. Estimating the amount of gas hydrate and free gas from marine seismic data. *Geophysics* **2000**, *65*, 565–573. [CrossRef]
6. Chen, M.P.; Riedel, M.; Hyndman, R.D.; Dosso, S.E. AVO inversion of BSRs in marine gas hydrate studies. *Geophysics* **2007**, *72*, C31–C43. [CrossRef]
7. Dai, J.; Snyder, F.; Gillespie, D.; Koesoemadinata, A.; Dutta, N. Exploration for gas hydrates in the deepwater northern Gulf of Mexico: Part I. A seismic approach based on geologic model, inversion and rock physics principles. *Mar. Petr. Geol.* **2008**, *25*, 830–844. [CrossRef]
8. Dai, J.; Banik, N.; Gillespie, D.; Dutta, N. Exploration for gas hydrates in the deepwater, northern Gulf of Mexico: Part II. Model validation by drilling. *Mar. Petr. Geol.* **2008**, *25*, 845–859. [CrossRef]
9. Dutta, N.C.; Dai, J. Exploration for gas hydrates in a marine environment using seismic inversion and rock physics principles. *Lead. Edge* **2009**, *28*, 792–802. [CrossRef]
10. Shelander, D.; Dai, J.; Bunge, G. Predicting saturation of gas hydrates using pre-stack seismic data, Gulf of Mexico. *Mar. Geophys. Res.* **2010**, *31*, 39–57. [CrossRef]
11. Shelander, D.; Dai, J.; Bunge, G.; Singh, S.; Eissa, M.; Fisher, K. Estimating saturation of gas hydrates using conventional 3D seismic data, Gulf of Mexico Joint Industry Project Leg II. *Mar. Petr. Geol.* **2012**, *34*, 96–110. [CrossRef]
12. Fohrmann, M.; Pecher, I.A. Analysing sand-dominated channel systems for potential gas-hydrate-reservoirs using an AVO seismic inversion technique on the Southern Hikurangi Margin, New Zealand. *Mar. Petr. Geol.* **2012**, *38*, 19–34. [CrossRef]
13. Zhang, Z.J.; McConnell, D.R.; Han, D.H. Rock physics-based seismic trace analysis of unconsolidated sediments containing gas hydrate and free gas in Green Canyon 955, Northern Gulf of Mexico. *Mar. Petr. Geol.* **2012**, *34*, 119–133. [CrossRef]
14. Dewangan, P.; Mandal, R.; Jaiswal, P.; Ramprasad, T.; Sriram, G. Estimation of seismic attenuation of gas hydrate bearing sediments from multi-channel seismic data: A case study from Krishna-Godavari offshore basin. *Mar. Pet. Geol.* **2014**, *58*, 356–367. [CrossRef]
15. Qadrouh, A.; Carcione, J.M.; Salim, A.M.; Harith, Z.Z.T. Attenuation effects on the seismic response of a bottom-simulating reflector. *J. Nat. Gas Sci. Eng.* **2015**, *24*, 510–517. [CrossRef]
16. Ehsan, M.I.; Ahmed, N.; Khalid, P.; Liu, X.W.; Naeem, M. An application of rock physics modeling to quantify the seismic response of gas hydrate-bearing sediments in Makran accretionary prism, offshore, Pakistan. *Geosci. J.* **2016**, *20*, 321–330. [CrossRef]
17. Han, D.; Batzle, M. Gain function and hydrocarbon indicators. In Proceedings of the SEG Annual Meeting, Dallas, TX, USA, 26–31 October 2003.
18. Russell, B.H.; Hedlin, K.; Hilterman, F.J. Fluid-property discrimination with AVO: A Biot-Gassmann perspective. *Geophysics* **2003**, *68*, 29–39. [CrossRef]
19. Russell, B.H.; Gray, D.; Hampson, D.P. Linearized AVO and poroelasticity. *Geophysics* **2011**, *76*, C19–C29. [CrossRef]
20. Zong, Z.Y.; Yin, X.Y.; Wu, G. Direct inversion for a fluid factor and its application in heterogeneous reservoirs. *Geophys. Prospect.* **2013**, *61*, 998–1005. [CrossRef]
21. Yin, X.Y.; Cao, D.P.; Wang, B.L.; Zong, Z.Y. Research progress of fluid discrimination with pre-stack seismic inversion. *Oil Geophys. Prospect.* **2014**, *49*, 22–34, 46. [CrossRef]
22. Zhang, S.; Huang, H.D.; Dong, Y.P.; Yang, X.; Wang, C.; Luo, Y.N. Direct estimation of the fluid properties and brittleness via elastic impedance inversion for predicting sweet spots and the fracturing area in the unconventional reservoir. *J. Nat. Gas Sci. Eng.* **2017**, *45*, 415–427. [CrossRef]
23. Ciz, R.; Shapiro, S.A. Generalization of Gassmann equations for porous media saturated with a solid material. *Geophysics* **2007**, *72*, 75–79. [CrossRef]
24. Aki, K.; Richards, P.G. *Quantitative Seismology*, 2nd ed.; W. H. Freeman and Co: New York, NY, USA, 2002.

25. Carcione, J.M. AVO effects of a hydrocarbon source-rock layer. *Geophysics* **2001**, *66*, 419–427. [CrossRef]
26. Guo, Z.Q.; Liu, C.; Li, X.Y.; Lan, H.T. An improved method for the modeling of frequency-dependent amplitude-versus-offset variations. *IEEE Geosci. Remote Sens. Lett.* **2015**, *12*, 63–67. [CrossRef]
27. Guo, Z.Q.; Liu, X.W. Seismic rock physics characterization of anisotropic shale-a Longmaxi shale case study. *J. Geophys. Eng.* **2018**, *15*, 512–526. [CrossRef]
28. Yang, J.; Zhang, L.; Wang, J.S.; Xie, N.; Ma, N.; Zhang, H. Quantitative characterization of gas hydrate based on forward modeling. *Oil Geophys. Prospect.* **2020**, *55*, 419–425. [CrossRef]
29. Ba, J.; Carcione, J.M.; Cao, H.; Du, Q.Z.; Yuan, Z.Y.; Lu, M.H. Velocity dispersion and attenuation of P waves in partially-saturated rocks: Wave propagation equations in double-porosity medium. *Chin. J. Geophys.* **2012**, *55*, 219–231. [CrossRef]
30. Ba, J.; Xu, W.; Fu, L.; Carcione, J.M.; Zhang, L. Rock anelasticity due to patchy saturation and fabric heterogeneity: A double double-porosity model of wave propagation. *J. Geophys. Res. Solid Earth* **2017**, *122*, 1949–1976. [CrossRef]
31. Ba, J.; Zhao, J.; Carcione, J.M.; Huang, H. Compressional wave dispersion due to rock matrix stiffening by clay squirt flow. *Geophys. Res. Lett.* **2016**, *43*, 6186–6195. [CrossRef]
32. Sun, W.T.; Xiong, F.S.; Ba, J.; Carcione, J.M. Effects of ellipsoidal heterogeneities on wave propagation in partially saturated double-porosity rocks. *Geophysics* **2018**, *83*, 71–81. [CrossRef]
33. Carcione, J.M. *Wave Fields in Real Media: Wave Propagation in Anisotropic, Anelastic, Porous and Electromagnetic Media*, 3rd ed.; Elsevier: Amsterdam, The Netherlands, 2015.